Optical Gain Characteristics of BGaAs/GaP Quantum Wells

Volume 12, Number 4, August 2020

Herbert S. Mączko
Robert Kudrawiec
Marta Gladysiewicz

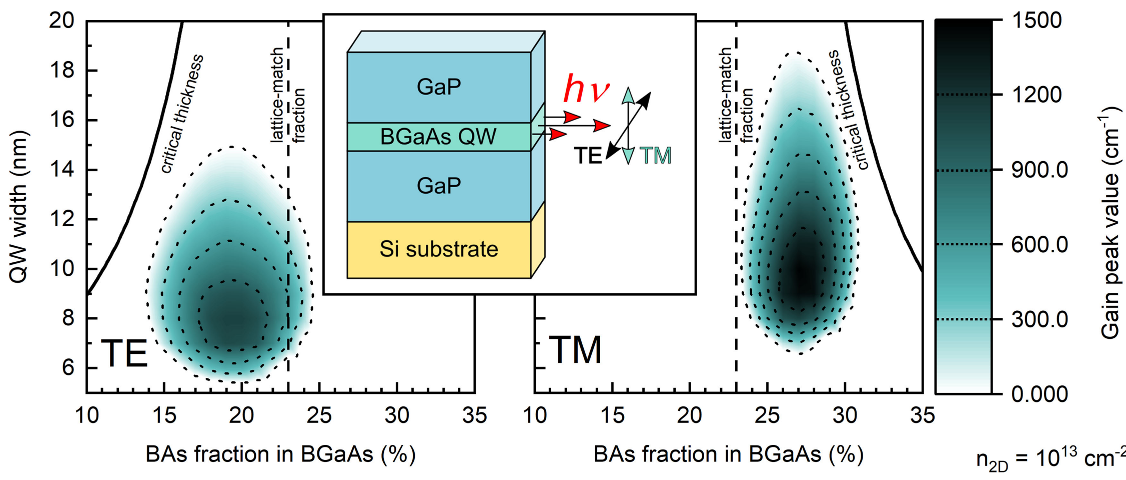

DOI: 10.1109/JPHOT.2020.3006624

Optical Gain Characteristics of BGaAs/GaP Quantum Wells

Herbert S. Mączko,[1] **Robert Kudrawiec**,[2] **and Marta Gladysiewicz**[1]

[1]Department of Experimental Physics, Faculty of Fundamental Problems of Technology, Wroclaw University of Science and Technology, Wrocław 50-370, Poland
[2]Department of Semiconductor Materials Engineering, Faculty of Fundamental Problems of Technology, Wroclaw University of Science and Technology, Wrocław 50-370, Poland

DOI:10.1109/JPHOT.2020.3006624
This work is licensed under a Creative Commons Attribution 4.0 License. For more information, see https://creativecommons.org/licenses/by/4.0/

Manuscript received April 7, 2020; revised June 24, 2020; accepted June 29, 2020. Date of publication July 2, 2020; date of current version July 17, 2020. This work was supported in part by National Science Center under Grant SONATA BIS 3 no. 2013/10/E/ST3/00520. The work of Robert Kudrawiec was supported by NCBiR within the Polish-China Grant WPC/130/NIR-Si/2018. Corresponding author: Herbert S. Mączko (e-mail: herbert.maczko@pwr.edu.pl).

Abstract: Light emitters integrated with Si platform are highly desirable for photonic integrated circuits, however, manufacturing them remains difficult. In this work, BGaAs/GaP quantum well (QW) structures are proposed as a promising solution of the challenge. These QWs can be grown on GaP/Si templates, which are intensively developed for recent years. An 8-band $\boldsymbol{k}\cdot\boldsymbol{p}$ model, envelope function approximation, self-consistency in solving of Schrödinger and Poisson equations with parabolic approximations of the indirect valleys and Fermi golden rule are used to calculate and analyze the material optical gain spectra of the QWs. A positive material gain is found for the QWs with 10–35% BAs mole fraction, with zinc-blende BGaAs epilayers grown on the GaP(001) substrates as direct gap semiconductors. It is predicted that such structures emit red light with wavelengths from the range of 730–690 nm. Optimal QWs widths for maximal TE and TM gain polarizations are below the critical thickness of BGaAs grown on the GaP(001). Presented results clearly indicate that BGaAs/GaP QW system is a very promising gain medium for Si-compatible photonic integrated circuits.

Index Terms: BGaAs, optical gain, modeling, quantum well, amplifying material, visible light source.

1. Introduction

The topic of light-emitting and lasing devices grown on Si wafers is of great interest among research groups focused on a silicon technology, because it can potentially allow production of new optoelectronic circuits with integrated light sources. Various approaches of manufacturing Si-integrated light-emitting devices have been already presented and gathered in reviews [1]–[4]. Recent and particularly interesting studies utilize GeSn alloys for which successful observations of photoluminescence and electroluminescence in the bulk crystals, thin epilayers, diodes and QWs all epitaxially grown on the Si substrates have been reported in experimental works [5], [6], [15], [7]–[14]. Furthermore, lasing actions of bulk crystals or QWs inside various micro resonators integrated with the Si technology have been demonstrated in recent studies [16]–[21]. Simultaneously with the advances in the technology, many theoretical researches predicted and analyzed

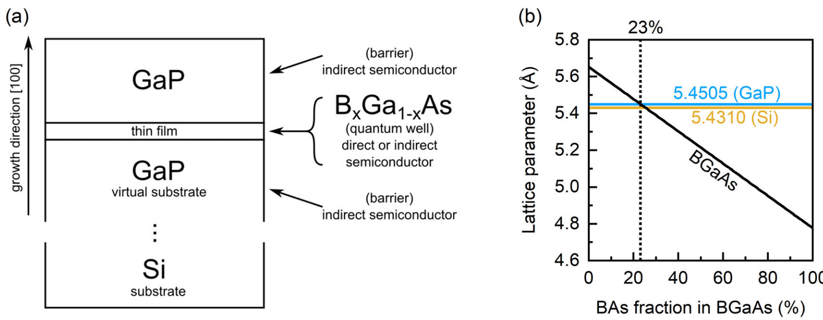

Fig. 1. (a) Schematics of the epitaxial structure with the modeled thin film forming single GaP/$B_xGa_{1-x}As$/GaP QW, (b) BGaAs lattice parameter dependency on BAs fraction in BGaAs (black solid line), lattice matching to GaP fraction (black dotted line), GaP, and Si lattice parameters (horizontal lines).

the optical gain of GeSn-based low-dimensional structures [22]–[29] to set up new possibilities in further development of the system. Other popular approaches are based either on silicon itself (Er doping, stimulated Raman scattering, Si nanoparticles) [3], [4], [30] or III-V semiconductor alloys that are already widely used in the light emitting applications (hybrid structures, heteroepitaxy of nanopillars or nanoneedles) [2], [3], [30]–[32].

Even though the topic of the Si-integrated light emitters is extensively researched, there still seems to be another new approach available. Despite the considerable difference in the lattice parameters between most of III-V binary compounds and Si, GaP crystal is characterized by the lattice parameter very similar to the one of Si [33], therefore allowing it to grow on Si with a good quality [34]–[36]. GaP for itself is not a suitable material to be an optical gain medium because it is an indirect-gap semiconductor [33]. Nonetheless, its wide gap creates a possibility for the manufacturing of quantum wells (QWs). In such QWs, GaP would form high barriers for electrons at the Γ point of the first Brillouin zone (BZ), and the thin film material additionally would have its conduction band minimum (CBM) at the Γ point below all of the CBMs of the GaP. Therefore, the material in search needs to fulfill these requirements. Recent advances in growth technology allow to produce new materials containing boron atoms, such as BGaAs, BGaP, BGaAsP, BGaInP, BGaInAs, BGaAsBi, BAsBi, on GaAs, Si and GaP substrates [37]–[40]. Before, these materials were often impossible to grow with a satisfying quality. From the group of materials considered, a BGaAs alloy is selected for this theoretical analysis as it consists of GaAs, a material that is well-known for its suitability for light applications and is one of the most developed semiconductors. Moreover, the alloy requires fewer mole fractions to be described compared to the quaternary alloys such as BGaAsP and BGaAsBi. The choice of BGaAs alloy for the QWs allows modelling a simple novel system that may be systematically extended to more complicated cases in further theoretical works. Similar quantum wells based on BGaAs already can be made on a GaAs substrate mostly. These types of quantum wells already have been explored experimentally [41]–[45]. A scheme illustrating BGaAs/GaP QWs is shown in Fig. 1(a). BGaAs alloys are characterized by the direct gaps in some BAs fraction range [46]–[49]. Their lattice parameter can be tuned to be close or equal to the one of GaP [33], [47], what is demonstrated in the Fig. 1(b). The investigated alloys form type I band offset with GaP [47], [48].

This research presents a new interesting material system for further experimental studies. It is based on theoretical calculations and prediction of material optical gain performed for the BGaAs/GaP QWs integrated with the GaP/Si virtual substrates at room temperature (300 K). We present and discuss estimations of characteristic features of these QWs including: band edge composition dependencies, an effect of partial carrier delocalization, an induced electric field effect on the optical gain values, and dependencies of the optical gain on the values of carrier concentration, BAs fraction, and QWs widths.

TABLE I
The Set of Material Parameters Used in the Calculations

Parameters	GaP	GaAs	BAs
Lattice parameters in 300 K			
a_{lc} (Å)	5.4505 [a, b]	5.65325 [a, b]	4.777 [b]
Valence band offsets & spin-orbit splittings			
VBO (eV)	– 1.27 [a]	–0.80 [a]	–0.95 [c]
Δ_{so} (eV)	0.08 [a]	0.341 [a]	0.22 [c]
Bandgaps at 0 K			
$E_g^{\Gamma,0}$ (eV)	2.886 [a]	1.519 [a]	5.5 [c]
$E_g^{\Delta,0}$ (eV)	2.35 [a]	1.981 [a]	1.93 [c]
$E_g^{L,0}$ (eV)	2.72 [a]	1.815 [a]	3.3 [c]
Varshni parameters			
α^{Γ} (meV/K)	—	0.5405 [a]	N.A.
β^{Γ} (K)	—	204 [a]	N.A.
α^{Δ} (meV/K)	0.5771 [a]	0.460 [a]	N.A.
β^{Δ} (K)	372 [a]	204 [a]	N.A.
α^{L} (meV/K)	0.5771 [a]	0.605 [a]	N.A.
β^{L} (K)	372 [a]	204 [a]	N.A.
Electron effective masses			
m_e^{Γ} (m_0)	0.114 [d]	0.067 [a, d]	0.1 [c]
$m_{e,DOS}^{\Delta}$ (m_0)	1.58 [d]	0.85 [d]	N.A.
$m_{e,DOS}^{L}$ (m_0)	0.75 [d]	0.56 [d]	N.A.
Luttinger's parameters			
γ_1	4.04 [d]	7.10 [d]	4.02 [e]
γ_2	0.53 [d]	2.02 [d]	0.04 [e]
γ_3	1.26 [d]	2.91 [d]	1.18 [e]
Deformation potentials			
a_c^{Γ} (eV)	—	– 9.3 [f]	– 14.2 [e]
a_v^{Γ} (eV)	—	– 0.7 [f]	N.A.
b^{Γ} (eV)	—	– 2.0 [a]	– 4.5 [d]
E_1^{L} (eV)	—	– 2 [d]	N.A.
E_1^{Δ} (eV)	—	1.05 [d]	N.A.
E_2^{Δ} (eV)	—	6.5 [d]	N.A.
Elastic constants			
C_{11} (GPa)	—	1221 [a]	2860 [e]
C_{12} (GPa)	—	566 [a]	670 [e]
Permittivies (zero frequency limit)			
ϵ_r	11.11 [b]	12.44 [b]	9.9 [e]
Optical energies			
E_p (eV)	31.4 [a]	28.8 [a]	N.A.

2. Methods

2.1 Material Parameters

All material parameters critical for the calculations conducted are listed in the Table I, with names of parameters' groups and symbols of the parameters listed in the first column. In most cases, the interpolation of the parameters is held within Vegard's law. In case of spin-orbit splitting and energy gap at the Γ point, interpolation includes non-zero bowing parameters according to a well-known

phenomenological interpolation scheme (1),

$$P^{(AB)C}(x) = x \cdot P^{AC} + (1-x) \cdot P^{BC} - x \cdot (1-x) \cdot b^{(AB)C} \tag{1}$$

where $P^{(AB)C}(x)$ is a given parameter of the alloy with a fraction x in an $A_xB_{1-x}C$ alloy, P^{AC} and P^{BC} are parameters for proper binary compounds, and $b^{(AB)C}$ is the bowing parameter for the alloy.

Parameters of GaP and GaAs are listed in the second and the third columns of the Table I. The majority of parameters is taken from the review publication of Vurgaftman *et al.* [47] except for parameters of and in connection to effective masses. For Luttinger parameters and all effective masses Adachi [46] seems to be the most accurate source of reference. The permittivity for both materials are taken from Madelung [33]. Hydrostatic deformation potentials of band extrema at the Γ point for GaAs are taken from experimental work of Nolte *et al.* [50], whereas deformation potentials for L and Δ valleys are taken from Adachi [46]. Deformation potentials and strain related parameters for GaP are not required for the purpose of this study and therefore are not presented in the Table I. There are no Varshni parameters given for GaP bandgap at the Γ point because its temperature dependence is properly described by (2) [47].

$$E_g^{\Gamma,T} = E_g^{\Gamma,0} + 0.1081 \cdot \left(1 - \coth\frac{164}{T}\right) \tag{2}$$

Parameters of BAs are listed in the fourth column of the Table I. Lattice parameter for BAs is taken from Madelung [33]. The bandgap energies are taken from calculations reported by Hart & Zunger [48], similarly to the valence band offsets (VBO) for BAs/GaAs interface. The VBOs of GaP and GaAs, unlike the VBO of BAs, are taken from the work of Vurgaftman *et al.* [47], therefore the VBO of BAs needs to be shifted so that it is consistent with the description of the remaining materials. In this study, the shift to VBO of BAs is implemented in such a way that the VBOs of GaAs reported in both works are equal. Luttinger coefficients and hydrostatic deformation potential for $\Gamma_{1c} - \Gamma_{4v}$ direct gap together with elastic constants and permittivity are reported in theoretical work of Chimot *et al.* [49]. And finally, Shear deformation potential b is taken from Adachi [46].

BGaAs alloys are still under development, therefore some of their material parameters are yet not available (N.A.), well established or available calculations require further experimental confirmation [51], [52]. Since hydrostatic deformation potentials of BAs are not yet known separately for conduction Γ_{1c} and valence Γ_{4v} bands, the hydrostatic deformation potential for the top valence band is 0 eV and the gap deformation potential [49] describes only the conduction band for the purpose of this study. An effective mass of electrons at the Γ_{1c} band (characterized by the same symmetry as the first conduction band in GaAs) is estimated by fitting a parabola to the band structure published by Hart & Zunger [48]. Despite of the lack of the remaining few parameters, we conducted our simulations approximating them to the ones of GaAs. The choice seems justified as the calculations concern lower BAs fractions in BGaAs alloys and are regarded as the preliminary predictions for the QWs.

A bowing parameter for the spin-orbit splitting energy 0.06 eV is taken from DFT calculations performed by Polak *et al.* [52] and for the energy gap at the Γ point 3.5 eV we quote Hart & Zunger [48]. The valence band offset (VBO) for the BGaAs alloys is interpolated linearly as its bowing parameter is not yet established.

2.2 Critical Thickness

We use (3), in accordance with Mathew-Blackslee model [53], to estimate the critical thickness of the thin BGaAs film grown on the GaP(100) virtual substrate and caped with another GaP crystal.

$$h_c = \frac{a_{film}}{2\sqrt{2}\cdot\pi\cdot f} \cdot \frac{1 - 0.25\cdot\nu}{1+\nu} \cdot \left(\ln\frac{\sqrt{2}\cdot h_c}{a_{film}} + 1\right)$$

$$f = \frac{|a_{sub} - a_{film}|}{a_{film}}, \qquad \nu = \frac{C_{12}}{C_{11} + C_{12}} \tag{3}$$

The dislocation angles and the burger vector are already substituted with he values specific for III-V alloys, h_c is the critical thickness, a_{sub} is the lattice parameter of the GaP substrate, a_{film} is the lattice parameter of the BGaAs thin film, C_{11} and C_{12} are elastic parameters of the BGaAs thin film. It is worth noting that this model underestimates the critical thickness, which can be larger in real structures. Real critical thickness is ruled by kinetic limitation of growth temperature and deposition rate [54].

2.3 Gain Calculation Procedure

Similarly to our previous works [22], [23], [55], [56], band-structures of bulk crystals are obtained within the 8-band $\boldsymbol{k}\cdot\boldsymbol{p}$ model for zinc-blende symmetry including the Bir-Pikus Hamiltonian for strain effects [57]. Here, the strain in the thin layer is homogenous with the unstrained substrate as its source. To calculate the band-structures of QWs, we used the above model including the envelope-function approximation [58]. The envelopes are expanded in a planewave basis, so the calculations are performed within periodic boundary conditions.

The bulk DOS functions of the L and Δ valleys are calculated within the effective mass approximation [59] using (4), where $D(E)$ is the DOS function, E is the energy, and m^* is the DOS effective mas of the given valley including the number of its equivalent minima. For the BGaAs thin film, both L and Δ valleys are shifted hydrostatically but only Δ valleys are additionally split into two groups due to simulation of the growth on the (100) plane. This effect is included in accordance to the model-solid theory [60]. Therefore, (4) is multiplied by the proper coefficient 1/3 or 2/3 and the energies are properly shifted for Δ valleys. A histogram based on 8-band $\boldsymbol{k}\cdot\boldsymbol{p}$ band structures is calculated to obtain DOS function, including states from the proximity of the Γ point. Local density of states (LDOS) of free carriers, which is included in the simulated structures, is described by band structures around Γ, Δ and L points for GaP, and around Δ and L points for strained BGaAs thin films. BGaAs bands around the Γ point are not included in the LDOS since their contribution will be added via confined states. A LDOS function describing the states confined in the QWs is determined by the calculation of the histogram in the energy space, that is weighted by the squared envelope functions of each found state. Both considered LDOS functions of free carriers and confined states are added to each other, then used in following calculations of the quasi-Fermi levels of conduction and valence bands with 2-dimensional carrier concentrations defined for whole period of the structure taken as parameters.

$$D(E) = \frac{1}{\pi^2} \cdot \left(2 \cdot \frac{m^*}{\hbar^2}\right)^{\frac{3}{2}} \cdot E^{\frac{1}{2}} \tag{4}$$

The carrier distributions are found with the quasi-Fermi levels and LDOS functions. Then, an induced electric field is calculated by solving the Poisson equation with Newton-Raphson method. Using the predictor-corrector based method [61], [62], Schrödinger and Poisson equations are self-consistently solved to properly include Δ valleys effect on the charge distribution in the structure and to find adequate final quasi-Fermi levels for the electrons. Next, the QWs band-structures are applied to the calculation of the material optical gain spectra of the QWs. The spectra are calculated within the standard approach based on the Fermi's golden rule [63], as in our previous works [22], [23], [55], [56].

3. Results and Discussion

3.1 Basic System Characterization

In the conceptual heterostructure, that is shown in the Fig. 1(a), the modelled single QW is formed by the $B_xGa_{1-x}As$ thin layer surrounded by the strain free GaP barriers. At the Γ point of the BZ, the system is characterized by type I band offset forming more than 0.5 eV deep quantum confinement for both holes and electrons. Because of the indirect nature of GaP crystal, the confining effect of holes in the system is much stronger than the one of electrons. Strain free GaAs is well known for

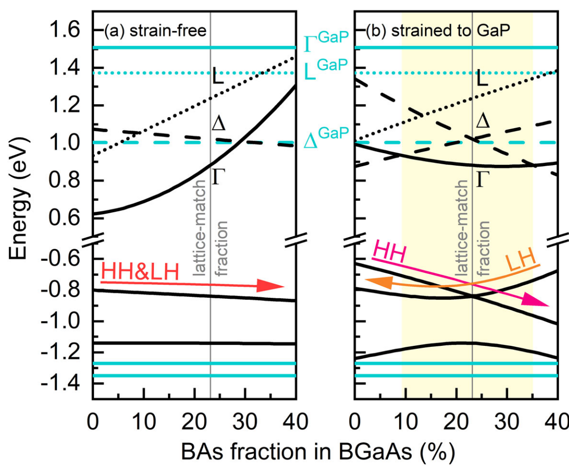

Fig. 2. Electron and hole energies at the Γ point (solid lines), electron energies in in L (dotted lines) and Δ (dashed lines) valleys minima as function of BAs mole fraction in $B_xGa_{1\text{-}x}As$ alloy at room temperature. Horizontal lines refer to the strain-free bulk GaP crystal while black lines refer to (a) the strain-free bulk $B_xGa_{1\text{-}x}As$ crystal, (b) the bulk $B_xGa_{1\text{-}x}As$ crystal strained to the GaP substrate. Vertical lines mark the fraction for which the alloy has the lattice parameter equal to the GaP one. The region colored in light yellow corresponds to the direct-gap $B_xGa_{1\text{-}x}As$ mole fractions for the strained crystal.

being a direct semiconductor, where the conduction band minima at the L point of BZ and at Δ line are around 0.3 eV and 0.5 eV above the Γ minimum. Whereas adding B to GaAs opens the bandgap, it also reduces the difference between indirect and direct conduction band minima. As a result, it creates an indirect semiconductor at the BAs mole fraction around 30%. The main reason to create such an alloy in this system is to reduce the elastic strain build-up in the $B_xGa_{1\text{-}x}As$ layers grown on the GaP substrate. There are two main benefits arising from this strain reduction. Firstly, a higher critical thickness is obtained. And secondly, the direct nature of the alloy is restored. GaAs strained to GaP when grown on the (100) plane acts as an indirect semiconductor with the low-energy group of Δ valleys around 0.1 eV below the Γ conduction band minimum. Addition of B in this case is necessary to reduce the effect of uniaxial deformations on the Δ valleys. Therefore, this alloying is necessary to have some electrons confined in the QW close to the Γ point instead of allowing all of them to leak into the Δ valleys.

The interpolations of the band extrema in Fig. 2 indicate that conduction band minima energy dependences on the BAs mole fraction are the most crucial for the system. As shown in Fig. 2(a), if the $B_xGa_{1\text{-}x}As$ alloy is a strain free material, there is potentially a wide range of mole fraction x for which a good confinement for electrons at the Γ point and a direct-gap character of semiconductor are present in the material. The situation changes noticeably when the strain effects are included, as shown in Fig. 2(b). At first, due to hydrostatic deformation the energy of electrons at the Γ point increases more than at the L point. In this way both energies for GaAs strained to GaP are almost equal. However, the energies of the Δ valleys are more important for the system than the energies of the L valleys. They would have similar importance as in unstrained case if only the hydrostatic deformation effect were present in GaAs. However, since the modeled structure is to be grown on the (100) plane, the significant Δ valleys splitting occurs and additionally limits the direct-bandgap fraction range. Hence, the most advantageous BAs mole fraction range, for QWs gain media, seems to span from 10 to 35%. For such BAs mole fraction range there is a direct gap in the $B_xGa_{1\text{-}x}As$ alloy. The indirect gap in GaP does not limit the applicable fraction range. The strain effect on the QWs depth at the Γ point for holes is insignificant for the confining ability. Still, its presence is easily visible in the fundamental optical transition energies and in the kind of holes forming the top valence band. Therefore, the strain only selects the radiation polarization for which optical gain takes positive values.

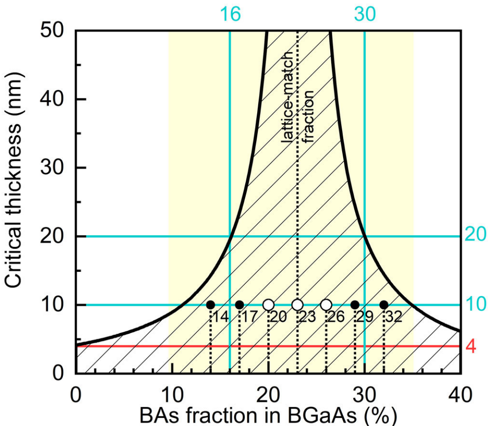

Fig. 3. Estimated critical thickness (thick black line) of the thin $B_xGa_{1-x}As$ film as grown on and covered by the GaP crystals, marked the 10 nm QWs with various BAs factions in the thin film that are chosen as most representatives for the optical gain analysis (black bordered white dots), other representative QWs (black dots). The region colored in light yellow corresponds to the direct-gap $B_xGa_{1-x}As$ mole fractions as in Fig. 2.

Another important parameter of the system is the critical thickness of the $B_xGa_{1-x}As$ grown on GaP. Its value limits the technological development of the thin-film growth and hence marks the range of QW widths that can be considered during the modeling. Fig. 3 shows the critical thickness within the fraction range corresponding to the direct-gap alloy with values beginning at around 8 nm for around 10% and increase with BAs fraction due to the decrease of the lattice mismatch between the alloy and the substrate. After exceeding around 23% it decreases and reaches around 10 nm for 35%, which is an estimated fraction of high fraction direct-indirect transition in strained BGaAs. There are 7 plotted points at 10 nm for various fractions. These are representative QWs chosen for further analysis of the gain spectra. Points corresponding to the fractions of 20, 23 and 26% are considered to be the most representative QWs, since they are characterized by three distinct kinds of strain incorporated into the thin films.

The first part of the analysis focuses on the most representative QWs, beginning with a presentation of main features connected to the carrier confinement and the QW positive charging effect and followed by the gain spectra characteristics with their dependence on two-dimension carrier concentration n_{2D}. Next, we focus on analyzing the gain spectra for all representative QWs with the peak gain and conclude with peak gain maps in function of BAs fraction from 10 to 35% and the QWs width from 5 to 20 nm. The fraction range is marked by the yellow region in Figs. 2 and 3, and in most cases the QWs width does not exceed the estimated critical thickness limitations.

3.2 BGaAs/GaP/Si Quantum Wells Characteristics

A typical energy profile at the Γ point of the considered QWs is shown in Fig. 4(a), where an induced electric field corresponds to a positive charging effect of the thin film in reference to the surrounding material. This effect is caused by the higher localization ability of holes than the one of electrons. Local densities of carriers (LDOC) calculated with the carrier density $n_{2D} = 10^{13}$ cm^{-2} for most representative QWs are shown in Fig. 4(b). According to them, higher concentrations of confined holes than of confined electrons are present in the thin film. In all three cases, the energy confinement around Γ point is highly favorable for both kinds of carriers. However, the existence of Δ valleys causes leakages of electrons such that while three of hole sub-bands are already filled, only one electron sub-band around Γ point is. The electrons that occupy the Δ valleys can be found in the thin layer and its proximity with the higher density, and in the barriers with the lower one. That is because these valleys in the whole structure have similar energies. The carrier density, in and around the thin layer, is much higher for the holes than for the electrons because many electrons

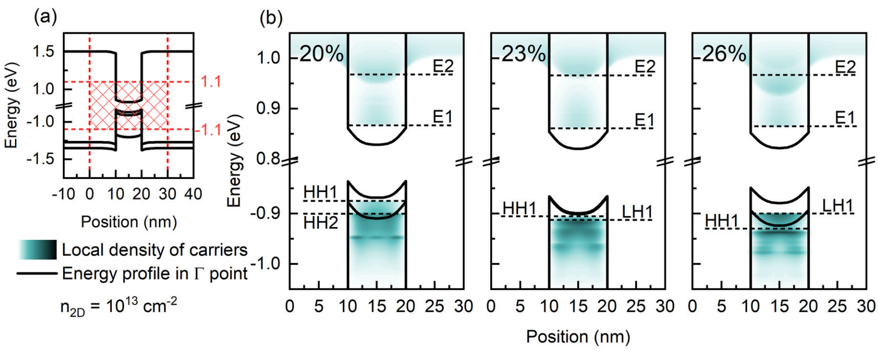

Fig. 4. (a) A typical GaP/$B_xGa_{1-x}As$/GaP single-QW energy profile with induced electric field, the energy and the position ranges of (b) figures (red patterned region). (b) most representative QWs Γ energy profiles (black solid lines), Γ energies of two first electron and two first hole states (black dashed vertical lines), LDOC (sea blue strikes) of both confined and free carriers in the system.

are distributed along the whole structure via the Δ valleys. It results in positive charging of the QWs surrounded by equivalent negatively charged barriers. This electric field allows a greater filling of the confined electron states, therefore favoring the positive gain values. So, additional characteristic features of this QW system are: a considerably smaller number of the electrons available for the radiative transitions than the holes and the induced electric field.

Concerning the relative energies of the Γ and the Δ valleys, the unstrained QWs are the most advantageous because there is no splitting of Δ valleys that would additionally lower its energy. Moreover, since the QW with the fraction 20% BAs is compressed by the GaP and the QW with the fraction 26% BAs is tensed, there is twice as many states available in the lowest Δ valley in the first QW. It makes higher fractions more attractive for light generation applications. However, because LDOC connected with the confined electrons are similar in shapes and in values in both cases, this effect is relatively small.

Some electrons from Δ valleys should be localized on the interfaces as an effect of the valleys energy position and the field induced in the QWs, what is visible in the LDOC charts. It is worth noting that carrier confinement or delocalization effects connected with Δ valleys are calculated with neglection of quantization effects in these valleys. Therefore, in a real device the leakage effects should be lower.

Many valence states are filled with holes while there is only one important conduction sub-band in the discussed QWs. The conduction sub-band always generates LDOC of the same shape and has almost constant electron filling level in all cases if the Δ valley is high enough. On the other hand, valence top sub-bands generate LDOS with shapes dependent on the BAs fraction, what induces different filling levels in each case. It is easy to notice, that for the most representative QWs the biggest ground-state hole density takes place in the strain-free QW. That is because the extrema of heavy-hole and light-hole sub-bands are closer in energy in this QW compared to the strained ones. However, it does not necessarily mean, that the highest gain values will appear in the case of the strain-free QW. The fraction of heavy and light holes included in the given LDOC is important for all cases when concerning the gain polarization. For example, the number of heavy holes close to the band edge is much smaller in the QWs with 20% of BAs in the film than the number of respective light holes in the QW with 26% of BAs. This is identified as the main reason of differences between the TE and the TM gain peak values of these QWs, which are presented in the following section.

3.3 Material Optical Gain Spectra Analysis

Figs. 5(a)–(c) shows that both polarizations, TE and TM, can dominate the gain spectra for two-dimensional carrier concentrations up to 12.0×10^{12} cm^{-2} for the most representative QWs. This

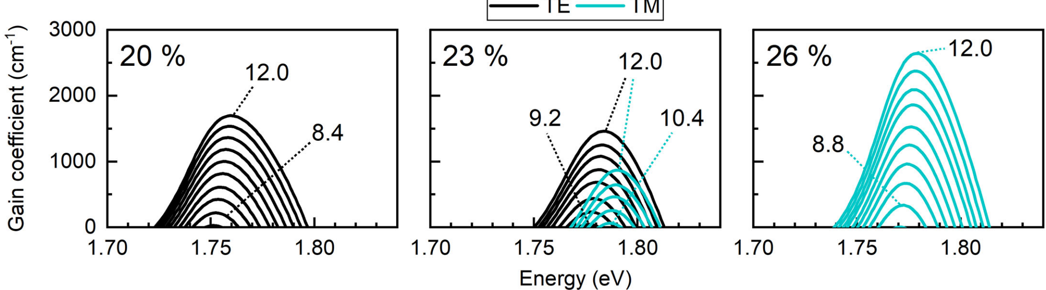

Fig. 5. Gain spectra of most representative QWs for TE (black solid lines) and TM (sea blue solid lines) radiation polarization. Gain spectra are calculated for 2-dimensional carrier concentrations n_{2D} up to 12.0×10^{12} cm^{-2} at room temperature. Neighboring lines are calculated for the concentrations differing by 0.4×10^{12} cm^{-2}.

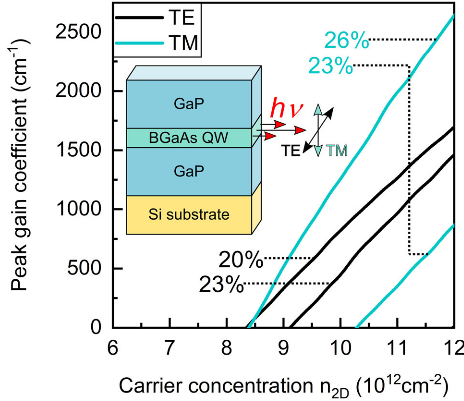

Fig. 6. Gain peak values of most representative QWs in function of 2-dimensional carrier concentration n_{2D} for TE (black solid lines) and TM (sea blue solid lines) radiation polarization.

is possible because various kinds of the hole sub-bands can become the top band for these QWs. In the case of the compressed QW (20% BAs), the top valence band can be filed with heavy holes that contribute only to the TE gain, as shown in Fig. 5(a). The gain spectra of both polarizations have positive values in case of the strain-free QW (23%), as shown in Fig. 5(b). It is apparent that the spectra for TE polarization of strain-free QW are similar in shapes and values to the spectra for the compressed QWs, however, their positive values begin at a higher carrier concentration. As presented in the previous section, the valence band LDOC close to the band edge is much higher for the unstrained QW than for the compressed one. Therefore, similar shapes of the TE gain spectra at higher concentrations mean that LDOC connected to the first heavy-hole sub-bands are very similar in these two QWs. The most apparent difference between these cases is connected to the light-hole sub-band present close to the top valence band in the strain-free QW. The minimal concentration of carriers for which positive values of the TE gain appear in the strain-free QW has a higher value than in the case of the compressed QW. This effect takes place as a result of a simultaneous filling of heavy and light-hole states instead of just the heavy ones. That is because the light-hole states are energetically close to the heavy-hole states. The TM gain values in the strain-free QW relate to the first light-hole sub-band and, as shown in Fig. 5(c), the TM radiation polarization dominates in the tensed QW. That is due to the high values of LDOC which appear close to the bands edge and their light-hole character.

To summarize the above discussion about the gain dependence on the carrier concentration, the peak gain is shown in Fig. 6. A first apparent feature when analyzing Fig. 6. is that the

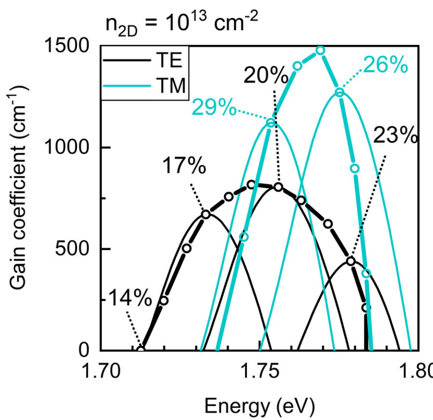

Fig. 7. Gain spectra (solid lines) of all representative QWs at room temperature for TE (black) and TM (sea blue) radiation polarizations, peak values and positions (open circles connected with thick solid lines) of 10 nm QWs with BAs mole fractions range covering the fractions of all representative QWs incremented by 1%.

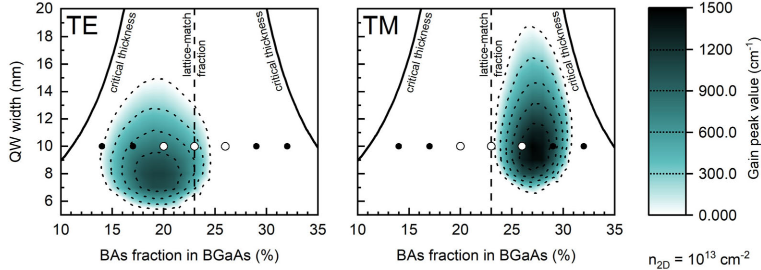

Fig. 8. Gain peak values (sea blue map) of QWs at room temperature in function of the QWs width and BAs mole fraction. For reference, critical thickness (solid black line), lattice match fraction (vertical line), representative QWs points (dots as in Fig. 3).

threshold carrier concentrations have an opposite dependency on BAs fraction for the TE and the TM polarizations. Consequently, the smallest carrier thresholds for TE polarization should be expected at lower fractions and for TM polarization at the higher ones. It is determined by the order in which valence sub-bands are filled with holes. It is difficult to precisely identify the source of the QWs fractions and polarization slope dependencies. Its cause may be either the first conduction state filling rate moderated by the Δ valley existence or the shapes of the hole LDOS functions. It is also worth noting that filling the second confined state does not contribute to the gain intensity since the optical transition between the first electron and the second hole level is not allowed.

Gain spectra of all representative QWs for the carrier concentration n_{2D} cover energy range from approximately 1.7 eV to 1.8 eV, as shown in Fig. 7. Consistently with the previous observations, the highest possible values of the gain can be obtained for TM polarization. However, the TE gain spectra covers wider energy range than the TM spectra. The same applies to the gain peak energies which vary from 1.71 to 1.79 eV for TE, and from 1.74 to 1.79 eV for TM polarizations. Moreover, TE gain spectra covers wider fraction range than TM spectra. Furthermore, an addition of B shifts the TE gain spectra toward higher energies while shifting the TM gain spectra toward the lower energies. It is related to the previously described strain effects on the valence bands.

Finally, the peak gain in function of the mole fraction and in the widths are exhibited in Fig. 8, where the parameters of optimal QWs for TE or TM polarizations can be predicted. It is visible that the peak values have their maxima separated by a fraction of around 8% while the width is comparable in both cases. Moreover, positive TM gain values appear at greater QW widths

because they are related to light-hole states. The fraction ranges of positive TE alone, TM alone and TE mixed with TM gain values are estimated to be respectively 14-24%, 23-31% and 23-24% BAs. A promising prediction is that both obtained optimal sets of parameters for TE and TM gain are found below the estimated critical thickness.

4. Conclusion

In this study, BGaAs/GaP QWs grown on the GaP/Si virtual substrates are proposed as a promising optical gain media for light emitters and carefully theoretically analyzed within the multiband $\boldsymbol{k}\cdot\boldsymbol{p}$ method. The band edge composition dependencies including the strain effect show that BGaAs grown on GaP(100) substrates is a direct-gap material in the reasonable range of BAs fraction that can be used for the QW growth. In addition, this paper highlights the importance of Δ valleys in generating electric field around the QWs. It is shown that for various BAs fractions in BGaAs diverse carrier concentrations are necessary to obtain positive values of the gain, affecting the threshold currents. Optimal BAs fractions in QWs are predicted to range from 14% to 31% and optimal widths are likely to be lower than the critical thickness. Red light (730–690 nm) emission from such structures may be expected. Therefore, it is explicit that the positive material gain can be achieved in the BGaAs/GaP QWs within the reasonable thickness and BAs fraction ranges. Consequently, this material system is very promising for Si-compatible photonic integrated circuits. Since the growth of BGaAs QWs is under development it is challenging to compare the obtained results to experimental data. Even more, this study is among pioneer works investigating BGaAs QWs and therefore have no other theoretical predictions to compare with. In other words, the presented results are the first road map for the development of BGaAs/GaP quantum wells for laser applications.

References

[1] T. T. Tran, J. Mathews, and J. S. Williams, “Towards a direct band gap group IV Ge-based material,” *Mater. Sci. Semicond. Process.*, vol. 92, no. May 2018, pp. 39–46, Mar. 2019.

[2] J. M. Ramirez *et al.*, “III-V-on-silicon integration: From hybrid devices to heterogeneous photonic integrated circuits,” *IEEE J. Sel. Top. Quantum Electron.*, vol. 26, no. 2, pp. 1–13, Mar. 2020.

[3] Z. Zhou, B. Yin, and J. Michel, “On-chip light sources for silicon photonics,” *Light Sci. Appl.*, vol. 4, no. 11, pp. 1–13, 2015.

[4] Z. Fang and C. Z. Zhao, “Recent progress in silicon photonics: A review,” *ISRN Opt.*, vol. 2012, pp. 1–27, 2012.

[5] J. Mathews *et al.*, “Direct-gap photoluminescence with tunable emission wavelength in $Ge_{1\text{-}y}Sn_y$ alloys on silicon,” *Appl. Phys. Lett.*, vol. 97, no. 22, pp. 2–5, 2010.

[6] M. Oehme *et al.*, “Room-temperature electroluminescence from GeSn light-emitting pin diodes on Si,” *IEEE Photon. Technol. Lett.*, vol. 23, no. 23, pp. 1751–1753, Dec. 2011.

[7] R. Roucka, J. Mathews, R. T. Beeler, J. Tolle, J. Kouvetakis, and J. Menéndez, “Direct gap electroluminescence from Si/$Ge_{1-y}Sn_y$ p-i-n heterostructure diodes,” *Appl. Phys. Lett.*, vol. 98, no. 6, Feb. 2011, Art. no. 061109.

[8] R. Chen, H. Lin, Y. Huo, C. Hitzman, T. I. Kamins, and J. S. Harris, “Increased photoluminescence of strain-reduced, high-Sn composition $Ge_{1-x}Sn_x$ alloys grown by molecular beam epitaxy,” *Appl. Phys. Lett.*, vol. 99, no. 18, Oct. 2011, Art. no. 181125.

[9] S. A. Ghetmiri *et al.*, “Direct-bandgap GeSn grown on silicon with 2230 nm photoluminescence,” *Appl. Phys. Lett.*, vol. 105, no. 15, Oct. 2014, Art. no. 151109.

[10] F. Pezzoli, A. Giorgioni, D. Patchett, and M. Myronov, “Temperature-dependent photoluminescence characteristics of GeSn epitaxial layers,” *ACS Photon.*, vol. 3, no. 11, pp. 2004–2009, Nov. 2016.

[11] C.-Y. Lin *et al.*, “Photoluminescence and electroluminescence from Ge/strained GeSn/Ge quantum wells,” *Appl. Phys. Lett.*, vol. 109, no. 9, Aug. 2016, Art. no. 091103.

[12] C. S. Fenrich *et al.*, “Strained Pseudomorphic $Ge_{1-x}Sn_x$ multiple quantum well microdisk using SiN_y stressor layer,” *ACS Photon.*, vol. 3, no. 12, pp. 2231–2236, Dec. 2016.

[13] T. R. Harris, M.-Y. Ryu, Y. K. Yeo, B. Wang, C. L. Senaratne, and J. Kouvetakis, “Direct bandgap cross-over point of Ge 1-y Sn y grown on Si estimated through temperature-dependent photoluminescence studies,” *J. Appl. Phys.*, vol. 120, no. 8, Aug. 2016, Art. no. 085706.

[14] W. Du *et al.*, “Investigation of optical transitions in a SiGeSn/GeSn/SiGeSn single quantum well structure,” *J. Appl. Phys.*, vol. 122, no. 12, Sep. 2017, Art. no. 123102.

[15] D. Stange *et al.*, “Short-wave infrared LEDs from GeSn/SiGeSn multiple quantum wells,” *Optica*, vol. 4, no. 2, pp. 185–188, 2017.

[16] S. Wirths *et al.*, “Lasing in direct-bandgap GeSn alloy grown on Si,” *Nat. Photon.*, vol. 9, no. 2, pp. 88–92, 2015.

[17] S. Al-Kabi *et al.*, "An optically pumped 2.5μm GeSn laser on Si operating at 110 K," *Appl. Phys. Lett.*, vol. 109, no. 17, p. 171105, Oct. 2016.
[18] D. Stange *et al.*, "Optically pumped GeSn Microdisk lasers on Si," *ACS Photon.*, vol. 3, no. 7, pp. 1279–1285, 2016.
[19] V. Reboud *et al.*, "Optically pumped GeSn micro-disks with 16% Sn lasing at 3.1 μm up to 180 K," *Appl. Phys. Lett.*, vol. 111, no. 9, Aug. 2017, Art. no. 092101.
[20] D. Stange *et al.*, "GeSn/SiGeSn heterostructure and multi quantum well lasers," *ACS Photon.*, vol. 5, no. 11, pp. 4628–4636, 2018.
[21] Y. Zhou *et al.*, "Optically pumped GeSn lasers operating at 270 K with broad waveguide structures on Si," *ACS Photon.*, vol. 6, no. 6, pp. 1434–1441, 2019.
[22] H. S. Mączko, R. Kudrawiec, and M. Gladysiewicz, "Strain engineering of transverse electric and transverse magnetic mode of material gain in GeSn/SiGeSn quantum wells," *Sci. Rep.*, vol. 9, no. 1, Dec. 2019, Art. no. 3316.
[23] H. S. Mączko, R. Kudrawiec, and M. Gladysiewicz, "Material gain engineering in GeSn/Ge quantum wells integrated with an Si platform," *Sci. Rep.*, vol. 6, no. 1, Dec. 2016, Art. no. 34082.
[24] Q. Zhang *et al.*, "Theoretical analysis of performance enhancement in GeSn/SiGeSn light-emitting diode enabled by Si_3N_4 liner stressor technique," *Appl. Opt.*, vol. 55, no. 34, Dec. 2016, Art. no. 9668.
[25] B. Dutt *et al.*, "Theoretical analysis of GeSn alloys as a gain medium for a Si-compatible laser," *IEEE J. Sel. Top. Quantum Electron.*, vol. 19, no. 5, 2013, Art. no. 1502706.
[26] G. Sun, R. A. Soref, and H. H. Cheng, "Design of an electrically pumped SiGeSn/GeSn/SiGeSn double-heterostructure midinfrared laser," *J. Appl. Phys.*, vol. 108, no. 3, Aug. 2010, Art. no. 033107.
[27] G.-E. Chang, S.-W. Chang, and S. L. Chuang, "Strain-balanced GezSn1-z-SixGeySn1-x-y multiple-quantum-well lasers," *IEEE J. Quantum Electron.*, vol. 46, no. 12, pp. 1813–1820, Dec. 2010.
[28] Y.-H. Zhu, Q. Xu, W.-J. Fan, and J.-W. Wang, "Theoretical gain of strained $GeSn_{0.02}/Ge_{1-x-y'}Si_xSn_{y'}$ quantum well laser," *J. Appl. Phys.*, vol. 107, no. 7, Apr. 2010, Art. no. 073108.
[29] S.-W. Chang and S. L. Chuang, "Theory of optical gain of Ge-$Si_xGe_ySn_{1-x-y}$ quantum-well lasers," *IEEE J. Quantum Electron.*, vol. 43, no. 3, pp. 249–256, Mar. 2007.
[30] Z. Fang, Q. Y. Chen, and C. Z. Zhao, "A review of recent progress in lasers on silicon," *Opt. Laser Technol.*, vol. 46, no. 1, pp. 103–110, 2013.
[31] K. Tanabe, K. Watanabe, and Y. Arakawa, "III-V/Si hybrid photonic devices by direct fusion bonding," *Sci. Rep.*, vol. 2, no. 1, pp. 1–6, Dec. 2012.
[32] J. C. Norman, D. Jung, Y. Wan, and J. E. Bowers, "Perspective: The future of quantum dot photonic integrated circuits," *APL Photon.*, vol. 3, no. 3, Mar. 2018, Art. no. 030901.
[33] O. Madelung, Ed., *Semiconductors*. Berlin, Heidelberg: Springer Berlin Heidelberg, 1991.
[34] T. J. Grassman *et al.*, "Control and elimination of nucleation-related defects in GaP/Si(001) heteroepitaxy," *Appl. Phys. Lett.*, vol. 94, no. 23, Jun. 2009, Art. no. 232106.
[35] T. J. Grassman *et al.*, "Nucleation-related defect-free GaP/Si(100) heteroepitaxy via metal-organic chemical vapor deposition," *Appl. Phys. Lett.*, vol. 102, no. 14, Apr. 2013, Art. no. 142102.
[36] A. Beyer *et al.*, "GaP heteroepitaxy on Si(001): Correlation of Si-surface structure, GaP growth conditions, and Si-III/V interface structure," *J. Appl. Phys.*, vol. 111, no. 8, Apr. 2012, Art. no. 083534.
[37] Q. Wang, X. Ren, H. Huang, Y. Huang, and S. Cai, "Growth of BxGa1−xAs, BxAl1−xAs and BxGa1−x−yInyAs epilayers on (001)GaAs by low pressure metalorganic chemical vapor deposition," *Microelectronics J.*, vol. 40, no. 1, pp. 87–91, Jan. 2009.
[38] N. Sommer *et al.*, "Growth of (BGa)As, (BGa)P, (BGa)(AsP) and (BGaIn)P by MOVPE," *J. Cryst. Growth*, vol. 370, pp. 191–196, May 2013.
[39] D. A. Beaton, A. J. Ptak, K. Alberi, and A. Mascarenhas, "Quaternary bismide alloy $B_yGa_{1-y}As_{1-x}Bi_x$ lattice matched to GaAs," *J. Cryst. Growth*, vol. 351, no. 1, pp. 37–40, Jul. 2012.
[40] S. R. Bank *et al.*, "Improved MWIR LED arrays on Si substrates for scene projectors," in *Proc. IEEE Res. Appl. Photon. Defense Conf.*, 2018, pp. 1–2.
[41] T. Hidouri *et al.*, "Engineering of carrier localization in BGaAs SQW for novel intermediate band solar cells: Thermal annealing effect," *Sol. Energy*, vol. 199, no. January, pp. 183–191, Mar. 2020.
[42] F. Saidi, R. Hamila, H. Maaref, P. Rodriguez, L. Auvray, and Y. Monteil, "Structural and optical study of BxInyGa1−x−yAs/GaAs and InyGa1−yAs/GaAs QW's grown by MOCVD," *J. Alloys Compd.*, vol. 491, no. 1–2, pp. 45–48, Feb. 2010.
[43] T. Hidouri, F. Saidi, H. Maaref, P. Rodriguez, and L. Auvray, "LSE investigation of the thermal effect on band gap energy and thermodynamic parameters of BInGaAs/GaAs single quantum well," *Opt. Mater. (Amst).*, vol. 62, pp. 267–272, Dec. 2016.
[44] A. You, M. A. Y. Be, and I. In, "Effect of boron incorporation on the structural and photoluminescence properties of highly-strained InxGa1-xAs/GaAs multiple quantum wells," *AIP Adv.*, vol. 3, no. 072111, pp. 1–13, 2013.
[45] R. Hamila, F. Saidi, H. Maaref, P. Rodriguez, and L. Auvray, "Photoluminescence properties and high resolution x-ray diffraction investigation of BInGaAs/GaAs grown by the metalorganic vapour phase epitaxy method," *J. Appl. Phys.*, vol. 112, no. 6, Sep. 2012, Art .no. 063109.
[46] S. Adachi, *Properties of Semiconductor Alloys: Group-IV, III – V and II – VI Semiconductors*. New York, NY, USA: Wiley, 2009.
[47] I. Vurgaftman, J. R. Meyer, and L. R. Ram-Mohan, "Band parameters for III-V compound semiconductors and their alloys," *J. Appl. Phys.*, vol. 89, no. 11 I, pp. 5815–5875, 2001.
[48] G. L. W. Hart and A. Zunger, "Electronic structure of BAs and boride III-V alloys," *Phys. Rev. B*, vol. 62, no. 20, pp. 13522–13537, 2000.
[49] N. Chimot, J. Even, H. Folliot, and S. Loualiche, "Structural and electronic properties of BAs and $B_xGa_{1-x}As$, $B_xIn_{1-x}As$ alloys," *Phys. B Condens. Matter*, vol. 364, no. 1–4, pp. 263–272, Jul. 2005.
[50] D. D. Nolte, W. Walukiewicz, and E. E. Haller, "Band-edge hydrostatic deformation potentials in III-V semiconductors," *Phys. Rev. Lett.*, vol. 59, no. 4, pp. 501–504, 1987.

[51] I. Gulyas, R. Kudrawiec, and M. A. Wistey, “Electronic structure of BxGa1−xAs alloys using hybrid functionals,” *J. Appl. Phys.*, vol. 126, no. 9, Sep. 2019, Art. no. 095703.

[52] R. Kudrawiec, M. P. Polak, K. M. McNicholas, J. Kopaczek, M. A. Wistey, and S. R. Bank, “Bowing of the band gap and spin-orbit splitting energy in BGaAs,” *Mater. Res. Express*, vol. 6, no. 12, Jan. 2020, Art. no. 125913.

[53] J. W. Matthews and A. E. Blakeslee, “Defects in epitaxial multilayers,” *J. Cryst. Growth*, vol. 27, no. DEC, pp. 118–125, Dec. 1974.

[54] D. D. Perović, B. Bahierathan, H. Lafontaine, D. C. Houghton, and D. W. McComb, “Kinetic critical thickness for surface wave instability vs. misfit dislocation formation in GexSi1-x/Si (100) heterostructures,” *Phys. A Stat. Mech. Its Appl.*, vol. 239, no. 1–3, pp. 11–17, 1997.

[55] M. Gladysiewicz, R. Kudrawiec, and M. S. Wartak, “Electronic band structure and material gain of III-V-Bi quantum wells grown on GaSb substrate and dedicated for mid-infrared spectral range,” *J. Appl. Phys.*, vol. 119, no. 7, pp. 1–11, Feb. 2016.

[56] M. Gladysiewicz, R. Kudrawiec, J. M. Miloszewski, P. Weetman, J. Misiewicz, and M. S. Wartak, “Band structure and the optical gain of GaInNAs/GaAs quantum wells modeled within 10-band and 8-band kp model,” *J. Appl. Phys.*, vol. 113, no. 6, Feb. 2013, Art. no. 063514.

[57] G. L. Bir and G. E. Pikus, *Symmetry and Strain-Induced Effects in Semiconductors*. New York, Toronto, Jerusalem, London: Willey, Israel Program For Scientific Translations, 1974.

[58] F. Szmulowicz, “Derivation of a general expression for the momentum matrix elements within the envelope-function approximation,” *Phys. Rev. B*, vol. 51, no. 3, pp. 1613–1623, 1995.

[59] P. Y. Yu and M. Cardona, *Fundamentals of Semiconductors Physics and Materials Properties*, 4th ed. Vienna, Austria: Springer, 2010.

[60] C. G. Van De Walle, “Band lineups and deformation potentials in the model-solid theory,” *Phys. Rev. B*, vol. 39, no. 3, pp. 1871–1883, 1989.

[61] A. Pacelli, “Self-consistent solution of the schröodinger equation in semiconductor devices by implicit iteration,” *IEEE Trans. Electron Devices*, vol. 44, no. 7, pp. 1169–1171, 1997.

[62] A. Trellakis, A. T. Galick, A. Pacelli, and U. Ravaioli, “Iteration scheme for the solution of the two-dimensional Schrödinger-Poisson equations,” *J. Appl. Phys.*, vol. 81, pp. 7880–7884, 1997.

[63] S. L. Chuang, *Physics of Optoelectronic Devices*, Illustrate. New York, Chichester, Brisbane, Toronto, Singapore: Wiley, 1995.